Electronic Supplementary Material 1

to the paper of

Constraints on the pre-eruptive magma storage conditions and magma evolution of the 56–30 ka explosive volcanism of Ciomadul (East Carpathians, Romania)

Cserép B, Szemerédi M, Harangi Sz, Erdmann S, Bachmann O, Dunkl I, Seghedi I, Mészáros K, Kovács Z, Virág A, Ntaflos Th, Schiller D, Molnár K, Lukács R

It contains additional information about the samples, supplementary figures and tables as well as the brief description of the thermobarometric, oxybarometric and chemometric methods applied in the paper.

1. Sample locations, petrography, geochemistry

Pumice samples were collected from representative outcrops of three well-defined explosive eruption events of Ciomadul. Locations of the outcrops are shown in Fig. 1. in the paper. Here we present details about the sampling localities, stratigraphic relations, and the key petrological and geochemical features.

Figure S1 *Sampling locations (stratigraphic unit names in red, eruption units in black): (a) Bixad roadcut, Ee5/2-32 eruption unit; (b) Băile Tuşnad roadcut, Ee5/1-50 eruption unit; (c) Covasna-Harghita frontier outcrop, Ee5/1-56 eruption unit; (d) Mohoş roadcut, Ee5/1-56 eruption unit. They all represent the youngest explosive eruptions (56–30 ka) of the Ciomadul volcanic complex. For unit and sample names, see the Samples section in the paper*

Eruption unit	Locality	Am (n)	Plg (n)	Zrn (n)	Ttn (n)	Mt (n)	Ilm (n)	Fe-Ti oxide eq. pairs (n)	Glass (n)
Ee5/2-32	Bixad	136	60	12	6	59	25	38	50
Ee5/1-50	Băile Tuşnad	46	55	9	4	26	8	26	15
Ee5/1-56	Covasna–Harghita front. Mohoş roadcut	118	119	9	6	86	22	43	67

Table S1 *Number (n) of the analysed spots for each mineral phase and the obtained Fe-Ti oxide pairs and silicate melt inclusions in the selected samples of the three studied eruption units. n= number of chemical analyses by EMPA or LA-ICP-MS*

Features	Ciomadul Mic (Kiss et al. 2014)	Ee5/1-56	Ee5/1-50	Ee5/2-32
Bulk-rock	trachydacite	dacite to trachydacite	dacite to trachydacite	dacite to trachydacite
Eruption type	effusive (lava dome)	explosive (pumice)	explosive (pumice)	explosive (pumice)
Crystal content (vol%)	31	10	9	19
Crystallinity (on vesicle-free basis, vol%)	33	27	29	38
Mineralogical assemblage	Plagioclase, amphibole, biotite (macrocrysts); apatite, zircon, titanite, Ti-magnetite/ilmenite (accessory phases); felsic crystal clots composed of plagioclase, amphibole, biotite, apatite, titanite and zircon occasionally with quartz and K-feldspar mafic crystal clots of olivine, clinopyroxene occasionally with plagioclase	Plagioclase, amphibole, biotite (macrocrysts); apatite, zircon, titanite, Ti-magnetite, ilmenite (accessory phases); occasionally orthopyroxene and clinopyroxene in mafic crystal clots	Plagioclase, amphibole, biotite (macrocrysts); apatite, zircon, titanite, Ti-magnetite, ilmenite (accessory phases); felsic crystal clots composed of plagioclase, amphibole, biotite, apatite, titanite and zircon	Plagioclase, amphibole, biotite (macrocrysts); apatite, zircon, titanite, Ti-magnetite, ilmenite (accessory phases)
Dominant plagioclase composition (An in mol%)	25–45	40–50	20–35	40–50
Amphibole	2 populations various reaction rims; 6.4–15.0 wt% Al_2O_3; 49–82 mol% Mg#	3 populations no reaction rim; 6.5–14.4 wt% Al_2O_3; 57–86 mol% Mg#	3 populations no reaction rim; 5.6–9.8 wt% Al_2O_3; 60–90 mol% Mg#	3 populations no reaction rim; 7.5–12.7 wt% Al_2O_3; 56–86 mol% Mg#

Table S2 *Summary of the key petrological and geochemical characters of the 133 ka old Ciomadul Mic lava dome rocks (Kiss et al. 2014) and the studied 56–30 ka old pumices*

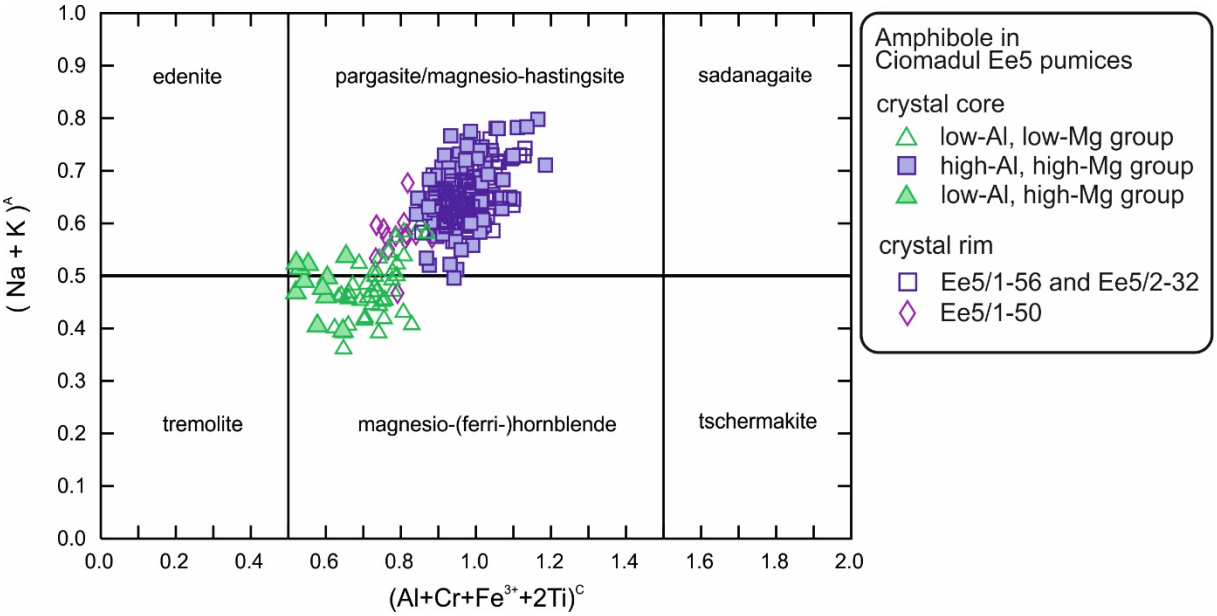

Figure S2 *Classification of amphiboles (Hawthorne et al. 2012; Locock 2014)*

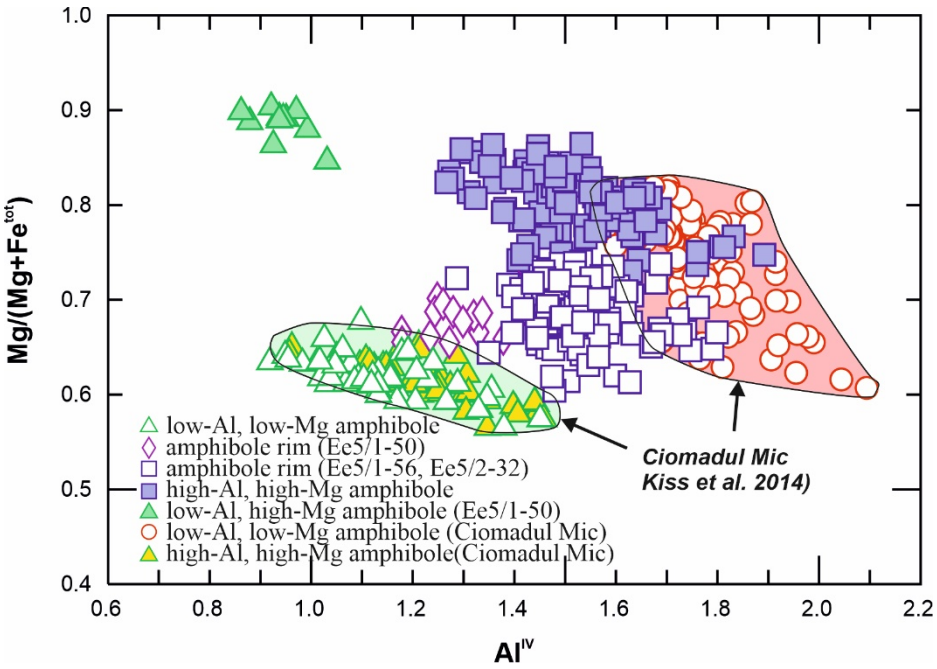

Figure S3 *Comparison of the amphibole composition from the 133 ka old Ciomadul Mic lava dome (Kiss et al. 2014) and from the studied pumice samples. Note the bimodal character of the lava dome samples, the larger compositional variation in the pumice samples, the similar compositional range of the low-Al, low-Mg amphibole and the distinct composition of the high-Mg amphibole population*

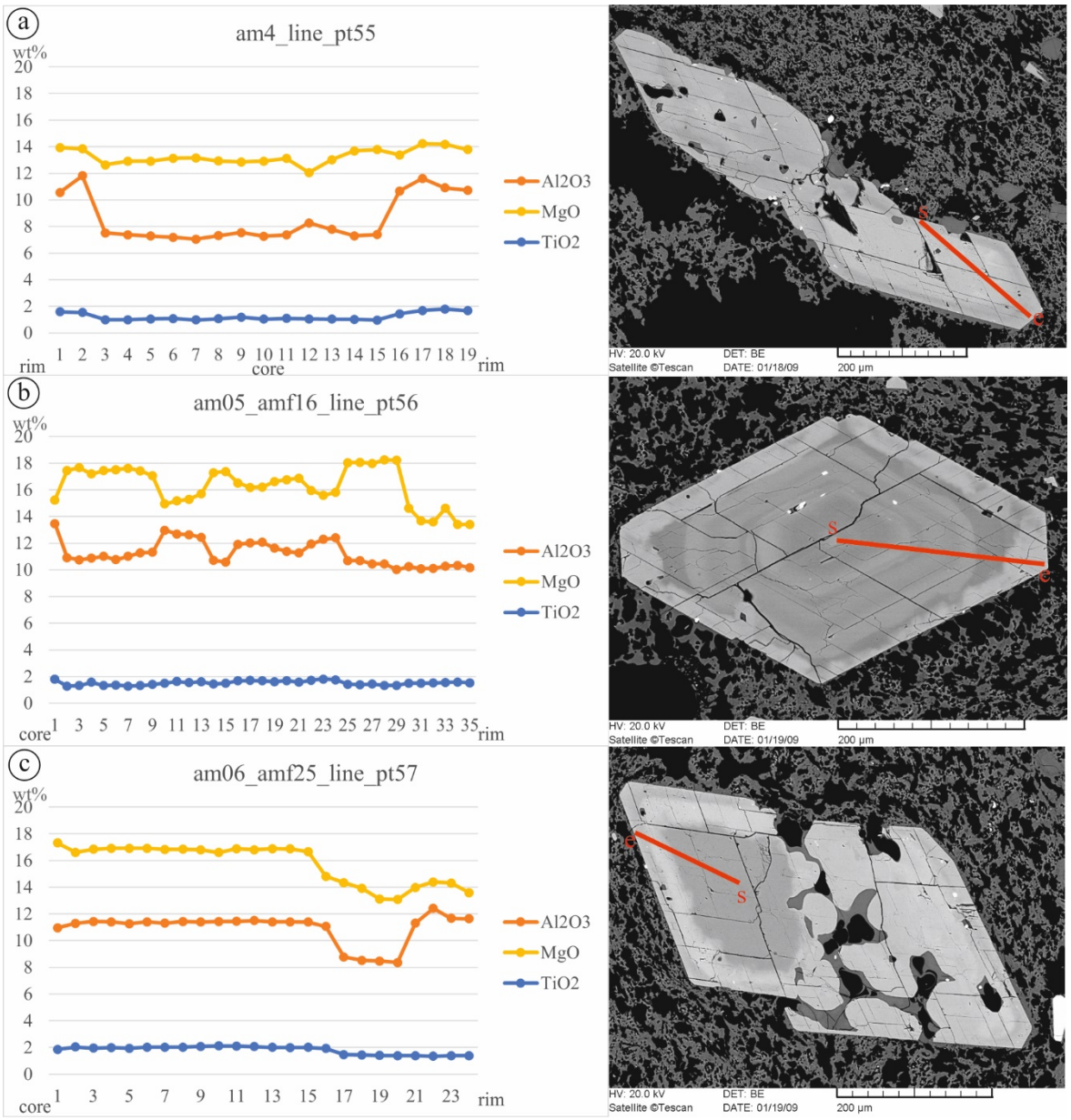

Figure S4 *Line profiles of a representative complex reverse zoned (a), an oscillatory zoned (b), and a complex normal zoned (c) amphibole crystal.*

2. Thermometers, barometers, oxybarometers and hygrometers used in the study

In the followings, we provide a summary of all the methods applied in the study, including their applicability according to the original papers, input parameters, calibration ranges, and inferred uncertainties. All the compositional input data are provided in the Electronic Supplementary Material 2 (ESM 2).

2.1. Fe-Ti oxide thermometers and oxybarometers (methods: Andersen and Lindsley 1985; Ghiorso and Evans 2008)

Temperature and fO_2 values were calculated on assumed equilibrium Ti-magnetite and ilmenite pairs using their homogeneous rim compositions (Fig. S5). Equilibrium was checked by magnetite-ilmenite Mg/Mn partitioning (cf. Bacon and Hirschmann 1988; Fig. S6). We employed the widely applied Andersen and Lindsley (1985) as well as the Ghiorso and Evans (2008) calibrations (abbreviated as oxAL85 and oxGE08, respectively). Both calibration methods require major element compositions of titanomagnetite-ilmenite equilibrium pairs determined by EMPA.

The oxAL85 calculations were performed using the WinMIgob software (Yavuz 2021). It can be used effectively in the Fe–Ti–O system between 600 and 1200 °C and a redox state between the NNO (nickel-nickel oxide oxygen) and the WM (wustite-magnetite) buffers. Ferric iron and Fe-Ti oxide end-members were calculated according to the method of Stormer (1983). This method has an inferred uncertainties of ±20–40 °C and ±0.5 log units fO_2 for temperature and oxygen fugacity, respectively (Andersen and Lindsley 1985; Yavuz 2021).

The oxGE08 calculation was performed using the Apple-based script of Ghiorso and Evans (2008). The method can be applied effectively to systems between 800 and 1300 °C, at an oxidation state of three log10 units on either side of the NNO buffer. Uncertainties are inferred to be ±25–50 °C and 0.2–0.3 log unit fO_2 for temperature and oxygen fugacity, respectively (Hayden and Watson 2007; Ghiorso and Evans 2008; Ghiorso and Gualda 2013; Loucks et al. 2020).

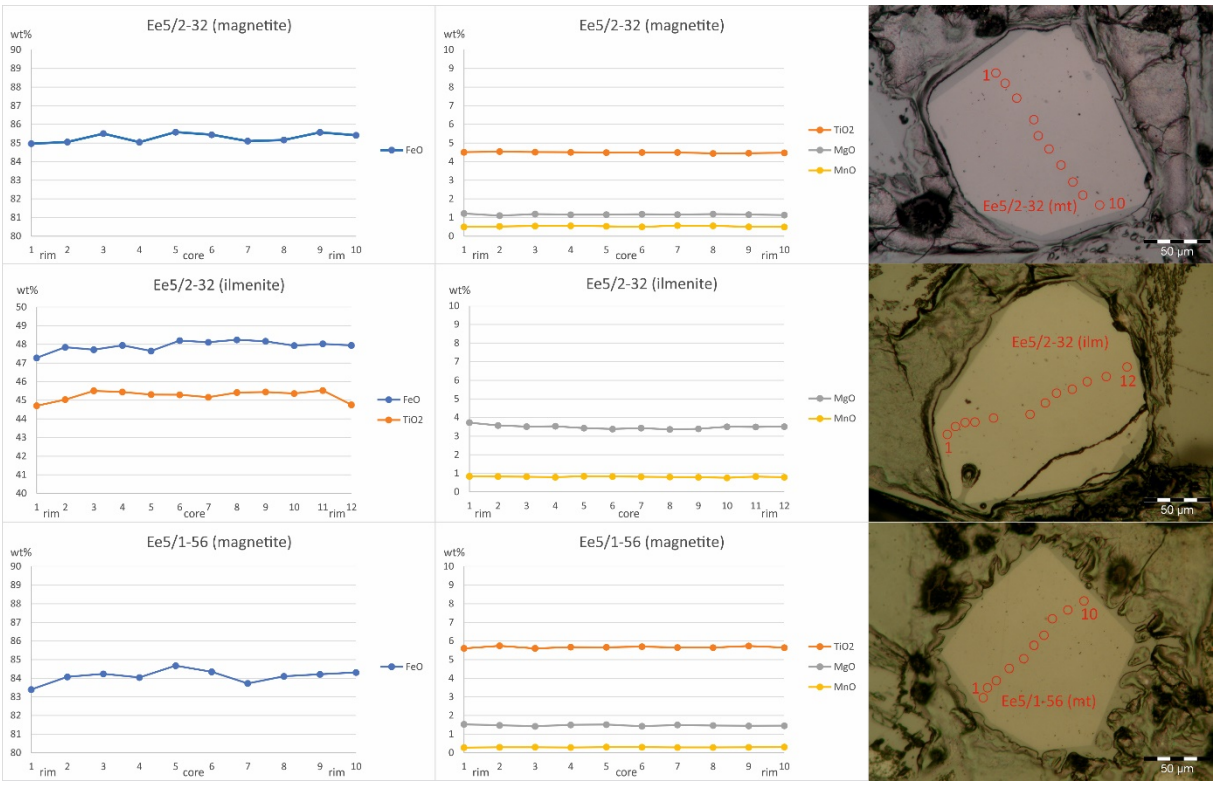

Figure S5 *Line profiles of some representative magnetite (a and c) and ilmenite (b) crystals*

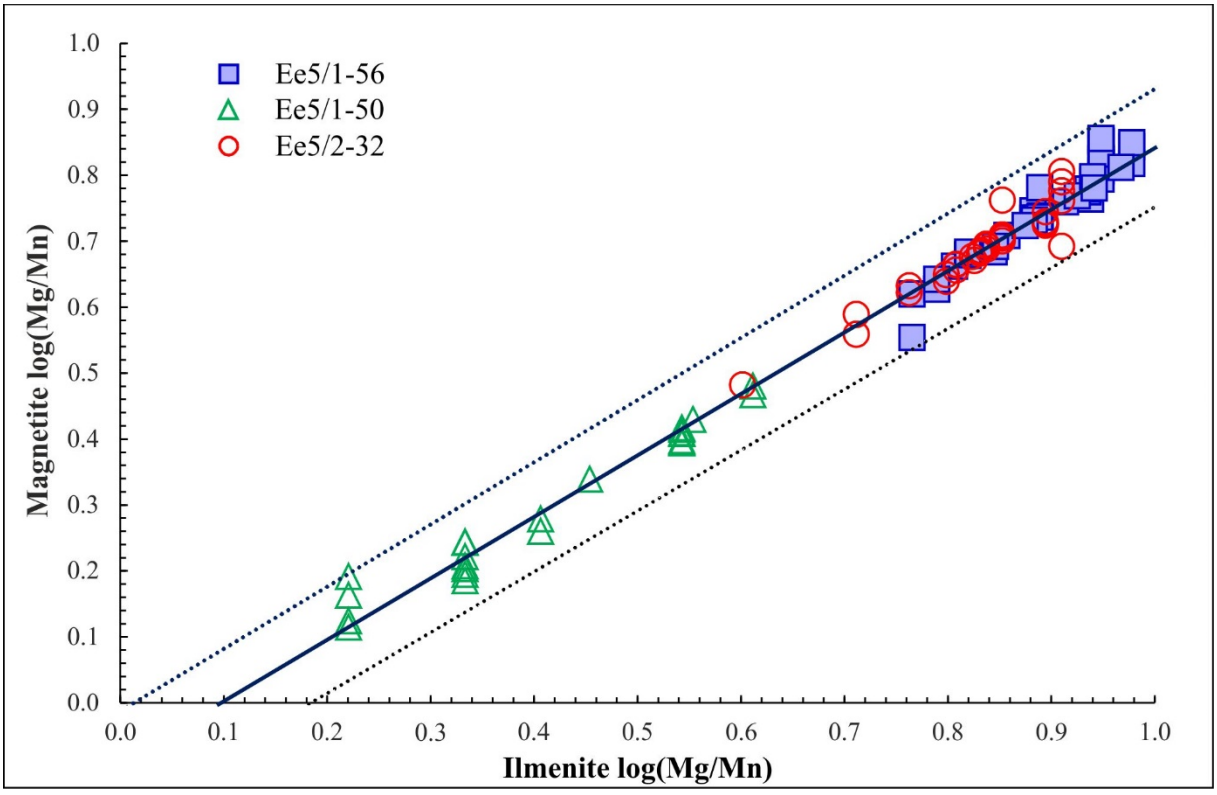

Figure S6 *Equilibrium test (Bacon and Hirschmann 1988) for titanomagnetite-ilmenite pairs from the three studied eruption units. Note the similar Mg and Mn contents of the Fe-Ti oxide pairs from the Ee5/1-56 and the Ee5/2-32 units, however, different concentrations characterize the Fe-Ti oxides of the Ee5/1-50 unit suggesting slightly different physicochemical conditions*

2.2. Amphibole±plagioclase thermobarometers, chemometers (Holland and Blundy 1994; Anderson et al. 2008; Krawczynski et al. 2012; Ridolfi and Renzulli 2012; Mutch et al. 2016; Putirka 2016; Ridolfi 2021; Higgins et al. 2022; Médard and Le Pennec 2022) and oxybarometers (Ridolfi et al. 2010)

Pre-eruptive temperature was calculated from rim compositions of inferred amphibole-plagioclase equilibrium pairs, where equilibrium was assessed based on textural observations. Crystal mush temperatures were calculated from compositions of low-Al, low-Mg amphibole and plagioclase pairs, where equilibrium was assumed between the euhedral amphibole inclusions and the host plagioclase and between the low-Al, low-Mg amphibole and plagioclase rims within felsic crystal clusters. We employed the Holland and Blundy (1994) edenite-richterite thermometer (hbHB94) for quartz-free assemblages, which requires amphibole and plagioclase major and trace element compositions as well as pressure as input parameters. The thermometer is applicable to Ca-amphiboles with 6.0–7.7 apfu Si, <1.8 apfu Al^{VI}, and X_{Na}^{M4}>0.03, and plagioclase with 0.9>Xan>0.1, being suitable for our compositions. For amphibole compositions with ≤15.4 wt% FeO, as in case of our data, the uncertainty of the thermometer is estimated to be ±35–40 °C, if pressure can be accurately constrained (Holland and Blundy 1994). Temperature values were calculated using the Excel spreadsheet provided by Anderson et al. (2008).

To estimate the temperature of the mafic magmas, the Putirka (2016) method was applied on high-Mg# single crystal amphibole cores (Mg#>0.60). In case of the Putirka (2016) method, two different calculations, a pressure independent (5^{th} equation in Putirka 2016) and a thermometer fixed at 400 MPa (6^{th} equation in Putirka 2016), were used with cation numbers calculated from amphibole major element compositions based on 23 O atoms. The 400 MPa pressure was chosen based on the amphibole major element composition similar to amphiboles produced by experiments above >400 MPa (see *Chapters: Origin of the crystal cargo* and *Pressure* in the paper). We also used the calculated temperature together with the Si cation number (apfu) to estimate the SiO_2 content in the coexisting liquid (with a 3.6 wt% uncertainty). The thermometer is applicable (according to the original paper) to Ca-amphiboles crystallized between 50 and 2500 MPa and between 650 and 1200 °C with 5.5–8.5 apfu Si, <3 apfu Al^{tot} which is suitable for our compositions. The uncertainty of the thermometer is estimated to be 30 °C.

The Ridolfi and Renzulli (2012) method can be applied for a temperature range of 800–1130 °C, thus, only for the high-Al, high-Mg amphibole population described in *Chapter Amphibole* in the paper. The compositions in our database are suitable according to the

Ridolfi and Renzulli (2012) paper, however the estimation gave erroneous values for the crystal mush amphiboles (760–845 °C), probably caused by the differences in the calibrational amphibole equilibrium assemblage which contains pyroxene in contrast to ours, therefore, we estimated temperatures only for amphibole compositions with Mg#>0.60. We used EMPA data of these Mg-rich (Mg/(Mg+ Fe^{tot})>0.60) calcic amphibole cores as input to the excel sheets provided by the authors. The temperature estimate has an uncertainty of ±23.5 ºC.

In case of the Ridolfi (2021) method, we checked amphibole compositions using the spreadsheet of the original paper and major element compositions as input parameters to calculate temperature, pressure, oxygen fugacity and melt water content. This thermometer can be applied on Mg-rich calcic amphiboles in equilibrium with calc-alkaline or alkaline melts at 885–1130 °C, 130 to 2200 MPa, and oxygen fugacity between -2.1 and 3.6 ΔNNO, with uncertainties of ±44 °C, ±12%, ±0.3 log unit, and ±14 %, respectively. Mg-rich calcic amphibole data used in this method fulfilled the criteria, however the amphibole crystals within the calibrational data set are mostly in equilibrium with a mafic assemblage (containing olivine, pyroxene, and high-An plagioclase) which is not true in the case of our assemblage and show compositional shift compared with our data, therefore, we could not accept the results of this method.

The Higgins et al. (2022) machine learning-based method was used on single crystal high-Mg# amphibole cores to evaluate the temperature and pressure conditions of the mafic magma and also applied to single amphibole rims to estimate the pre-eruption conditions. One of the advantages of this method is that it uses a non-linear regression strategy, which provides a better fit with the experimental data set. Beside T and P, liquid composition in equilibrium with the amphibole was also calculated. The random forest thermobarometer using ExtraTrees package (Breiman 2002) together with code of R environment provided by the authors of the paper was applied. The method requires amphibole major element composition as input parameter and it can be applied on amphibole crystallized on 50–1200 MPa pressure and 700–1250 °C temperature conditions from basaltic to rhyolitic magma with wide compositional range, similarly to amphiboles given in this study. Although, the temperature of the experimental data set used in the calibration extends down to 700 °C, only few data from experiments between 700 and 800 °C are included in the training data set. Therefore, we accepted the results of this method only for amphibole cores with Mg#>0.60 crystallized above 800 °C. The uncertainties of the estimation are ±160 MPa pressure and ±40 °C temperature, while uncertainties for each element in the calculated melt composition are the

following: SiO_2: 3.3 wt%, Al_2O_3: 1.1 wt%, FeO: 1.5 wt%, MgO: 0.8 wt%, CaO: 1.3 wt%, Na_2O: 0.7 wt%, K_2O: 0.5 wt%, and TiO_2: 0.2 wt%.

Pressure was estimated also using the Anderson et al. (2008) spreadsheet (hbA08) with the Anderson and Smith (1995) iteration method (AS95), as well as the Mutch et al. (2016) Al-in-hornblende barometer (hbM16) from both crystal mush and pre-eruptive amphibole compositions used in the hbHB94 thermometer. Both requires Al^{tot} composition as an input parameter and an equilibrium assemblage of hornblende, biotite, plagioclase, orthoclase, quartz, titanite/ilmenite, magnetite, and ±apatite, and equilibration at <800 °C. In the pumiceous pyroclastic deposits, the mineral assemblage matches these requirements, except for orthoclase and quartz. We rigorously discuss this issue in the paper emphasizing that K-feldspar and quartz are present in the lava dome rocks as phenocrysts and in the felsic crystal clots representing the crystal mush in addition to the same mineral assemblage found also in the pumices. They have overlapping mineral composition and are assumed to represent the same long-standing crystal mush body. Furthermore, the K_2O content in the glass composition of the Ee5/1-56 and Ee5/2-32 units is close to 5 wt%, while the Ee5/1-50 pumice glass contains SiO_2 over 75 wt%, implying they are close to the K-feldspar and quartz saturation (according to Médard and Le Pennec 2022). Therefore, we accept the pressure values yielded by these geobarometers. The hbA08 barometer is applicable to hornblende crystallized at 250–1300 MPa, with an uncertainty of 60 MPa. The hbM16 barometer is applicable to hornblende crystallized at 80–1000 MPa with an inferred uncertainty of ±16 %.

The Médard and Le Pennec (2022) temperature-independent barometer was used on single crystal low-Al, low-Mg amphibole cores and on high-Al, moderate-Mg amphibole rims from EMPA major element input data. This method works at a condition when amphibole crystallizes together with plagioclase + biotite ± quartz ± magnetite ± sanidine at 650 to 950 °C, mostly under 400 MPa. Considering the crystallization condition of the low-Al, low-Mg and the high-Al, moderate-Mg amphiboles as discussed above, we accepted the pressure results of this barometer, which show low standard deviations for both groups and overlap with the results of the Mutch et al. (2016) method. The accuracy of the method is about ±72–86 MPa.

The empirical Mg# barometer provided by Krawczynski et al. (2012) can be applied for high-Mg amphibole with Mg-number between 0.74 and 0.84 crystallized preferably at 180–950 MPa. As input parameter, we used Al^{VI} cation numbers calculated from EMPA results using Equation 2 in the paper. The reported uncertainty of the amKr12 method is about ±142 MPa.

Oxygen fugacity was calculated from amphibole compositional data using the single amphibole oxybarometer and spreadsheet of Ridolfi et al. (2010). The calculation requires single amphibole major element composition as an input parameter (we used high-Al, moderate-Mg amphibole rims to determine conditions after hybridization; low-Al, low-Mg amphibole compositions for the long-term crystal mush) and it normally uses temperature and pressure calculated from the same composition. However, in these calculations we used the hbHB94 and the hbAS95 temperature and pressure values, respectively, as input parameters which were considered to be the most reasonable results for crystal mush condition. Results gained by the Ridolfi et al. (2010) method give good correspondence with the fO_2 values obtained by the Andersen and Lindsley (1985) calculations from Fe-Ti oxide pairs. The Ridolfi et al. (2010) oxybarometer is applicable to amphibole crystallized at ~750–1000 °C, <1000 MPa, an oxygen fugacity between 0.3 and 2.5 ΔNNO, a crystallinity <35%, amphibole Al-number (Al^{VI}/Al^{tot}) <0.21 apfu, and $Mg/(Mg+Fe^{2+})$>0.5, all of which criteria were fulfilled for most of the studied samples. An uncertainty of ±0.4 log units has been estimated for this method (Ridolfi et al. 2010) and additional tests showed that it gives reasonable values within this uncertainty (Erdmann et al. 2014).

2.3. Zircon thermometer and oxybarometer and zircon saturation temperature (Watson and Harrison 1983; Ferry and Watson 2007; Loucks et al. 2020; Crisp and Berry 2022)

We applied the Ti-in-zircon thermometer of Ferry and Watson (2007) to calculate the crystallization condition in the felsic crystal mush. Ti content of zircon rim composition was used as given by Lukács et al. (2021). The main uncertainty of this calculation (estimated to be about ±30–35 °C at 750 °C) is the unconstrained activities for SiO_2 and TiO_2. Lukács et al. (2021) discussed the crystallization condition and used a_{SiO2}=1 and a_{TiO2}=0.6 values, which we accepted in this study. Loucks et al. (2020) extended the equation provided by Ferry and Watson (2007) with a pressure dependence and therefore their calculations give higher temperature values (with about 50–70 °C) at 250 MPa pressure. The inferred uncertainty of the thermometer is ~±30 °C if all input parameters are accurate (Loucks et al. 2020). The Loucks et al (2020) method calculates also the oxygen fugacity under which the zircon crystallization occurred. It uses the concentrations of Ce, initial U, and Ti in the zircon grains as well as bulk rock composition (Molnár et al. 2019) as input parameters. The oxybarometer is inferred to calculate $\log fO_2$ with a standard error of ±0.6 log units (Loucks et al. 2020).

To calculate zircon saturation temperature, we used the zircon solubility model of Watson and Harrison (1983) and Crisp and Berry (2022) on zircon rim compositions. The

model of Watson and Harrison (1983) requires microprobe glass major element composition as well as the Zr content to calculate the melt cation ratio of (Na+K+2 Ca)/(Al*Si), and the Zr distribution coefficient. The model is applicable with wide range of melt composition from peraluminous to metaluminous, between 750 and 1020 °C, with alumina saturation index (ASI) of 0.90–1.10. For this calculation, we used the average glass Zr content determined by LA-ICP-MS method in Perugia, 160 ppm for the Ee5/1-56 and Ee5/2-32 units and 150 ppm for the Ee5/1-50 unit.

Crisp and Berry (2022) recently published another calibration to calculate zircon saturation temperature. It uses Zr concentration and major element composition of the glass and/or bulk rock and pressure to estimate zircon saturation temperature. It can be used between 750 to 1620 °C and 0.1 and 4000 MPa, where the ASI is between 0.20 to 2.0, the FeO^{tot} is 1–16 wt%, and the melt H_2O is 0–17 wt%. The uncertainty of the method is ±45 °C. We used the Excel spreadsheet provided by the authors with 250 MPa pressure value. It gave similar results to the Watson and Harrison (1983) calculation.

2.4. Titanite thermometer (Hayden et al. 2008) and barometer (Erdmann et al. 2019)

The Zr-in-titanite thermometer of Hayden et al. (2008) was used with an input data obtained by LA-ICP-MS analysis in Göttingen from various zones in titanite grains. Zr concentrations with fixed 250 MPa pressure, a_{SiO2}=1 and a_{TiO2}=0.6 were used in the calculation of temperature values. This thermometer can be applied on titanite crystallized between 600 and 1000 °C temperature and at 200–240 MPa pressure. The method has a ±20 °C given uncertainty. As in our mineral assemblage quartz/rutile is absent, the uncertainty could be larger affecting the results by 35 to 75 °C overestimation.

The semi-quantitative titanite barometer of Erdmann et al. (2019) requires the Al_2O_3 content of magmatic titanite as an input parameter, near-solidus crystallization of an equilibrium assemblage of Ca-amphibole, plagioclase, alkali feldspar, quartz, biotite, and magnetite/ilmenite. The barometer has been proposed for pressures between ~150 and 400 MPa for metaluminous to weakly peraluminous silicic magmatic systems. The estimated uncertainty of the barometer is ±60–100 MPa. We used this geobarometer with a consideration on the mineral assemblage as discussed above.

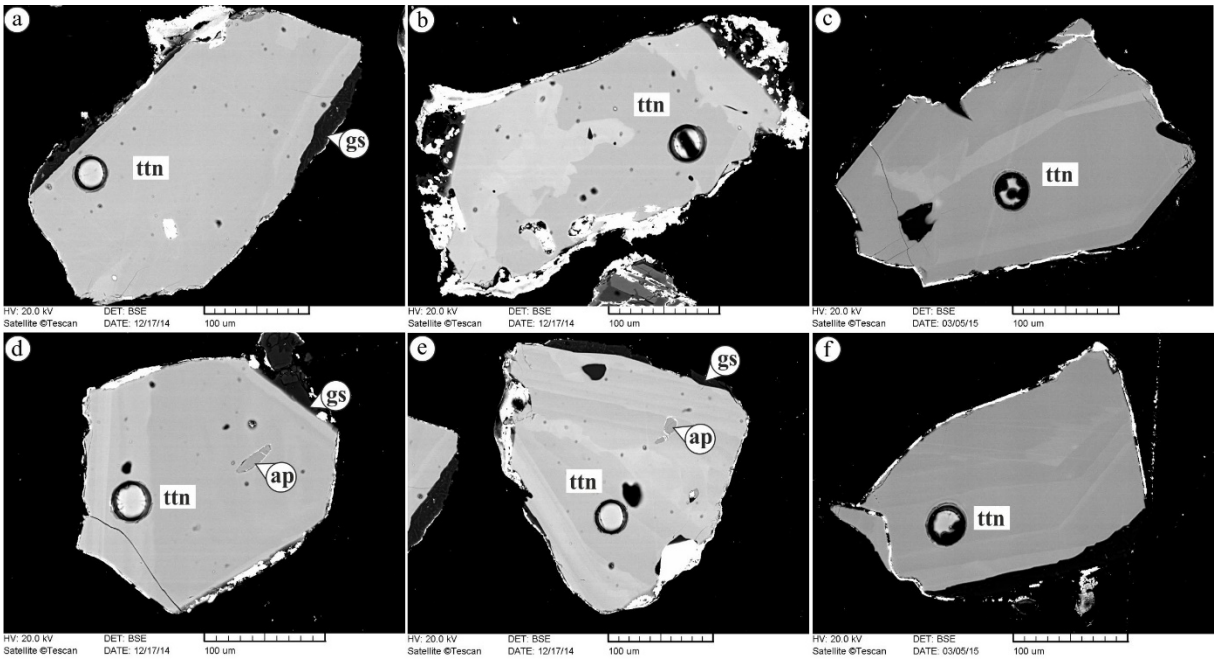

Figure S7 *High contrast back-scattered electron (BSE) images of titanite crystals separated from the Ee5/1-56 (a, e) and the Ea5/1-50 (b–d and f) eruption units, representing the prolonged crystal mush. Note the different textures from slight zonation (a, c) or resorbed core (b) to well-developed oscillatory zonation (d–f). Laser spots for trace element analysis are also shown*

2.5. Magnetite-melt oxybarometer (Arató and Audétat 2017a, b, c)

We applied two magnetite-melt oxybarometers of Arató and Audétat (2017a, b, c) on magnetite rims paired with matrix glass compositions. One of the oxybarometers is based on the partitioning of V between magnetite and the melt (Arató and Audétat 2017a, b), while the other uses the partitioning of Fe and Ti between magnetite and melt (FeTiMM method, Arató and Audétat 2017c). They require the V concentrations of the magnetite and melt, temperature, alumina saturation index (ASI) of the melt and the Fe and Ti concentrations of magnetite and melt and melt composition (AMCNK) as input parameters, respectively. The V-based oxybarometer is applicable for crystallization at 0.7–4.0 units above the fayalite-magnetite-quartz buffer (ΔFMQ), at 800–1000 °C, a melt ASI between 0.74 and 1.14, a magnetite composition with 0.2–14 wt% TiO_2, crystallization at 100–500 MPa, and H_2O saturation. The method is inferred to have an uncertainty of ±0.3 log units.

The FeTiMM method (Arató and Audétat 2017c) is calibrated for magnetite-melt equilibration at 750–1100 °C, 10–700 MPa, and fO_2 between -1.3 and +5.5 ΔFMQ, melt compositions of 48–79 wt% SiO_2, ASI=0.3–1.3, and magnetite compositions of 0.01–28 wt% TiO_2. It has an inferred uncertainty of ±0.5 log units.

2.6. Plagioclase-liquid hygrometer (Waters and Lange 2015)

The plagioclase-liquid hygrometer of Waters and Lange (2015) requires plagioclase and melt major and trace element compositions, temperature, and pressure as input parameters. We used plagioclase rim compositions paired with average microlite-lacking groundmass glass surrounding the plagioclase crystals (ESM 2) and estimated avarage rim temperatures (730°C in case of Ee5/1-50 and 810 °C in the Ee5/1-56 and Ee5/2-32 ka units; derived from the hbHB94 calibration) and pressure (250 MPa in case of Ee5/1-50; and 350 MPa in the Ee5/1-56 and Ee5/2-32 ka units, amphibole rim, derived from the hbMLP22 and the hbM16 calibrations) inserting in the Excel spreadsheet provided by the authors. The calibration can be applied to plagioclase crystallized from a wide magma composition including silicic magmas, for plagioclase compositions between An = 17 mol% and An = 95 mol%, crystallization pressures of 0–350 MPa, melt H_2O contents of 0–8.3 wt%, and temperatures of ~750–1250 °C. The given uncertainty of the method is ±0.35 wt%.

3. Output data of the applied methods

3.1. Amphibole-plagioclase equilibrium pairs

Coexisting amphibole-plagioclase pairs (e.g., Fig. S8) of the studied materials form two distinct groups. The first group involves high-Al, moderate-Mg amphibole and moderate An content plagioclase pairs. The crystals are 50–800 μm sized euhedral or sporadically subhedral macrocryst-couples, showing no or rarely step zonation in case of amphibole and slight diffusional zonation in case of plagioclase crystals, but in the latter case, we only used homogeneous domains within the crystal rims (similarly to Gorini et al. (2018)) with with low standard deviations for estimations (see details in ESM 2).

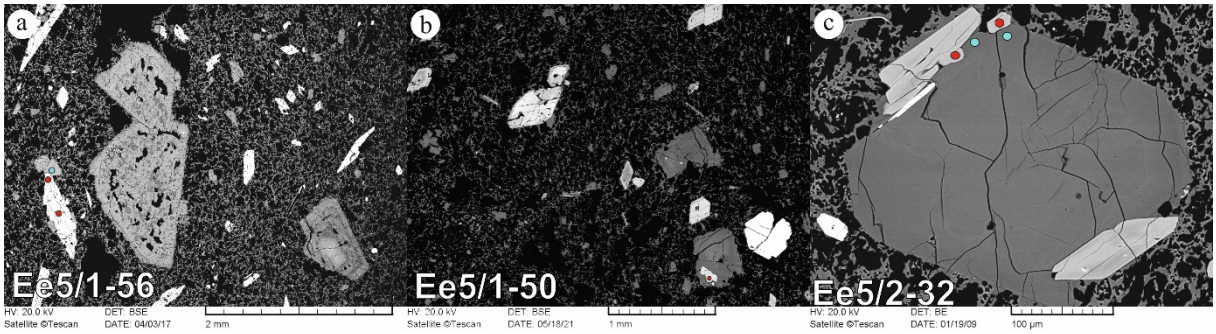

Figure S8 *Back-scattered (BSE) images of representative coexisting amphibole-plagioclase pairs with the analysed spots (red for amphibole and blue for plagioclase). Compositional data from the rims, close to the mineral boundaries were used for geothemometry calculations. a) Ee5/1-56 unit, b) Ee5/1-50 unit c) Ee5/2-32 unit*

In the Ee5/1-50 unit, plagioclase rim has An=0.2–0.4, while the amphibole rim has 1.2–1.4 apfu Al^{IV}. They do not form equilibrium pairs, therefore, regarding the pre-eruptive temperature we accepted only Fe-Ti oxide pair results. The Ee5/2-32 and the Ee5/1-56 units show differences from the Ee5/1-50 unit containing An=0.4–0.5 plagioclase crystals, which coexist with amphiboles having 1.4–1.8 apfu Al^{IV}. Altogether 54 amphibole-plagioclase pairs were selected for thermometry (amphibole rims paired with average plagioclase composition of An=0.43; Ab=0.54). The calculations using hbA08 and the hbMLP22 methods resulted in a temperature value range from 780 to 820 °C and pressure values from 340 to 455 MPa. The amphiboles from these units have fO_2 results between ΔNNO +1.0 and +1.5. These amphibole crystal rims have transitional compositions in the Mg# vs. Al^{IV} diagram and most probably represent the pre-eruption conditions.

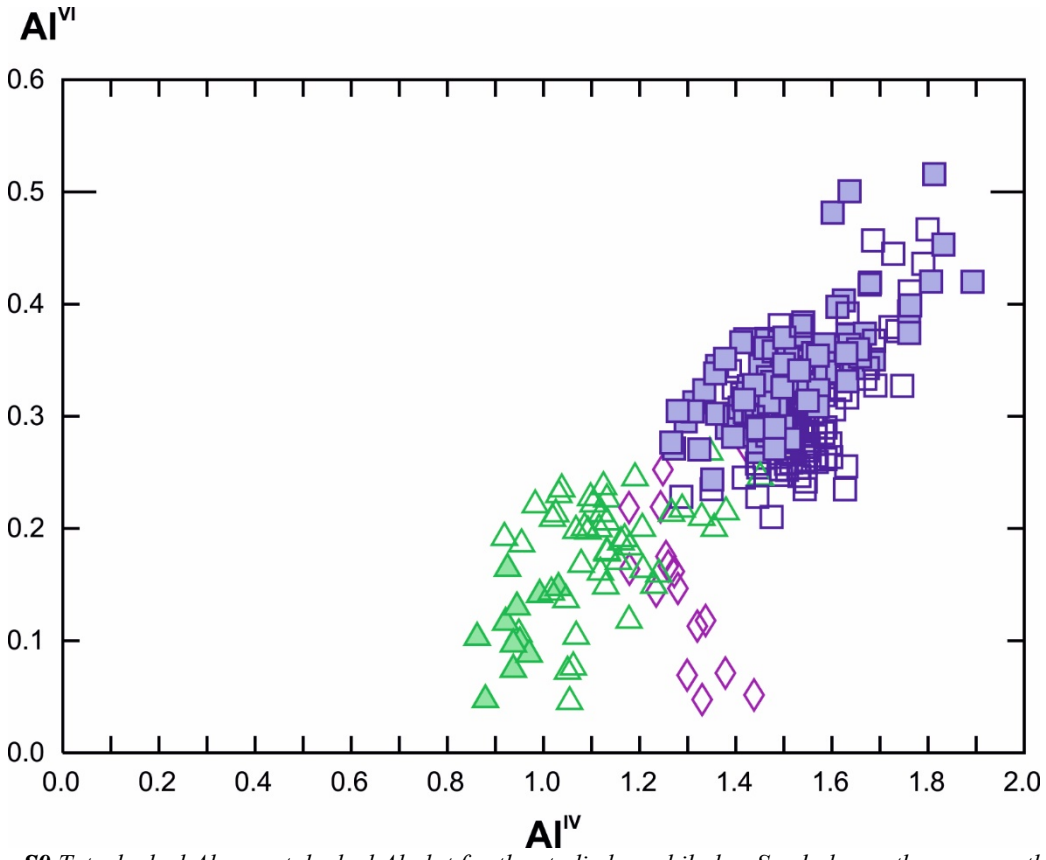

Figure S9 *Tetrahedral Al vs. octahedral Al plot for the studied amphiboles. Symbols are the same as those in Fig. S2*

The second amphibole-plagioclase group comprises low-Al, low-Mg amphibole with plagioclase having low anorthite content. The latter ones are typically larger crystals (>500 μm) and they include smaller (a few tens of μm) homogeneous amphibole inclusions. The host crystals usually show complex zonation. The inclusions occur mostly in the outer rim or occasionally in the core. In the Ee5/1-50 eruptive unit, plagioclase has An=0.2–0.3 and the

coexisting amphibole has 0.9–1.1 apfu Al^{IV}. Eleven amphibole-plagioclase pairs (amphibole rims paired with average plagioclase composition of An=0.26; Ab=0.71) were chosen to calculate the crystallization temperature. The calculations resulted in 690–720 °C temperature values and 210–280/165–290 MPa pressure values using the hbA08 and hbM16/hbMLP22 methods, while the single amphibole oxygen fugacity calculations gave fO_2 between ΔNNO +1.0 and +1.6. In the Ee5/2-32 and the Ee5/1-56 units, a few (18) amphibole-plagioclase pairs were found with 1.0–1.3 apfu Al^{IV} amphibole and An=0.3–0.5 plagioclase compositions (for calculation we used amphibole rims paired with average plagioclase composition of An=0.34; Ab=0.63). Using these mineral pairs, calculations resulted in a temperature and pressure range of 725–755 °C (hbA08) and 220–330/215–295 MPa (hbM16/hbMLP22), respectively. These amphiboles show oxygen fugacity between 0.9 and 1.4 ΔNNO.

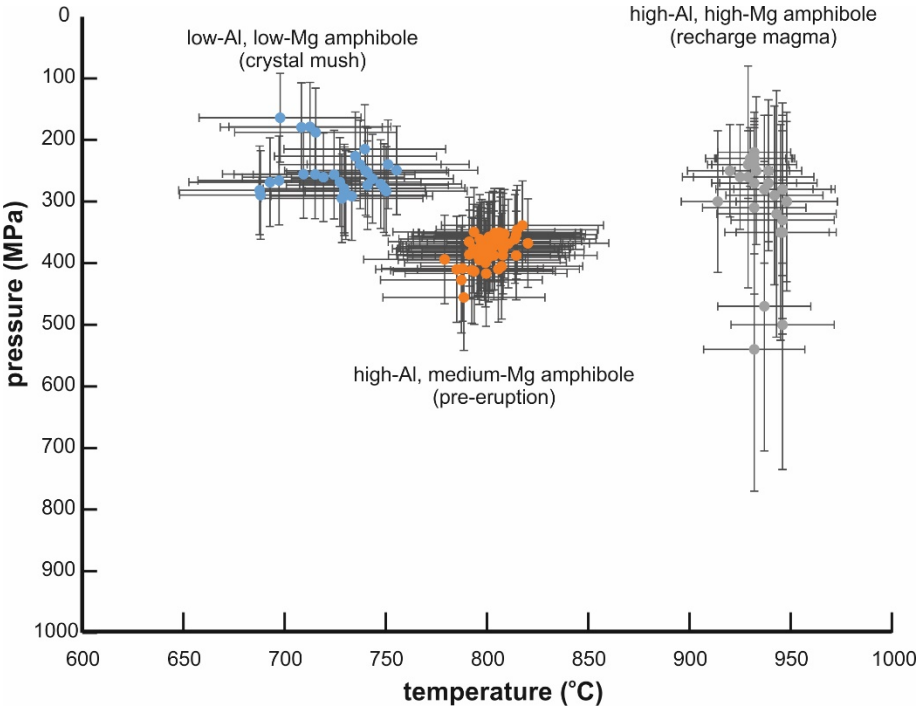

Figure S10 *Calculated pressure and temperature values for various amphibole type of Ciomadul pumices. For low-Al and low-Mg amphibole, thought to represent the felsic crystal mush environment and for the transitional (high-Al, medium-Mg) amphibole type temperature was calculated using the amphibole-plagioclase thermometer of Holland and Blundy (1994), while the pressure was calculated using the Médard and Le Pennec (2022) equation. For the high-Al, high-Mg amphibole type, representing the recharge magma, the Machine learning method of Higgins et al. (2022) was used to estimate the temperature and pressure. The pressure values, however, do not fit the textural observations, since this amphibole forms the crystal cores, has resorbed margin and is overgrown by transitional amphibole type. Therefore, we estimated the crystallization pressure based on experimental data.*

3.2. Fe-Ti oxides

From the three studied eruption units (Fig. 1, Fig. S1, Table 1, Table S1) 30 to 49 magnetite (mt) and 22 to75 ilmenite (ilm) crystals were analysed, in 35 to 89 and 22 to 76 spots, respectively. Line profile analyses (Fig. S5; in 5 to 11 spots/representative crystals)

proved the homogeneous compositions of the analysed Fe-Ti oxide grains with low standard deviations (see details in ESM 2). Overall, 26 to 43 mt-ilm equilibrium pairs/eruption unit were found and used for thermobarometric calculations. These numbers basically reach (or at least approach) the necessary numbers of magnetite and ilmenite analyses to obtain reliable Fe-Ti oxide temperatures with relatively low propagated uncertainties (≤±10 °C; Jolles and Lange 2019).

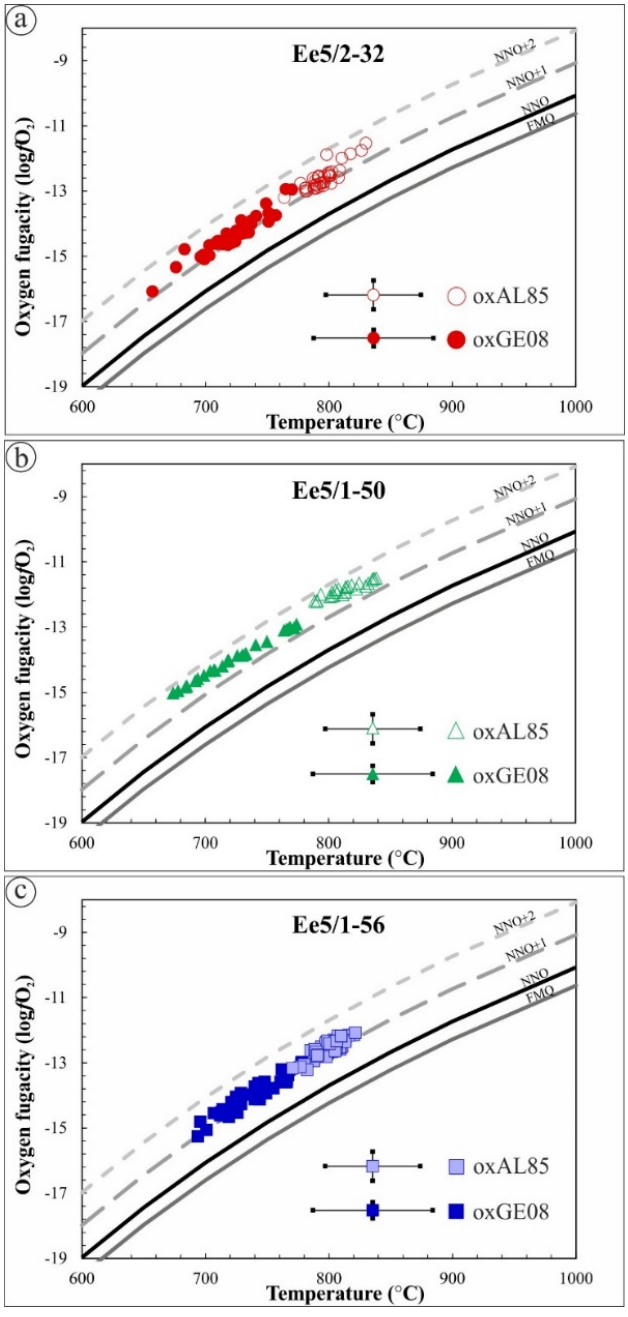

Figure S11 *Temperature (°C) and oxygen fugacity (logfO_2) results of the three studied eruption units (a–c) calculated by the Andersen and Lindsley (1985) and the Ghiorso and Evans (2008) Fe-Ti oxide geothermometers and oxygen barometers, using the WinMIgob (Yavuz 2021) and the Fe-Ti geothermometer (Ghiorso and Evans 2008) programs*

Temperature values calculated by the oxGE08 geothermometer are in the range between 660 and 780 °C and an average of ~730 °C. In contrast, calculations of the oxAL85 geothermometer resulted in systematically higher temperatures for all units (60–90 °C difference in average), having a range between 760 and 840 °C with lower standard deviations (avg. 13 °C) than the temperatures calculated by the oxGE08 geothermometer (avg. 25 °C).

Regarding oxygen fugacity, similar values were calculated by the oxGE08 and the oxAL85 methods. ΔNNO values from the oxGE08 thermobarometer are in the range between 0.8 and 1.7, while those of the oxAL85 method are between 0.9 and 1.9. Besides the notable overall similarity among the calculated parameters for the studied eruptive units, some differences can be highlighted. In case of fO_2, the Fe-Ti oxides from the Ee5/1-50 unit gave significantly higher values (i.e., more oxidizing condition) than the Fe-Ti oxide pairs from the other two units. On the other hand, no differences in the results can be observed for the Ee5/1-56 and the Ee5/2-32 eruptive units.

3.3. Zircon

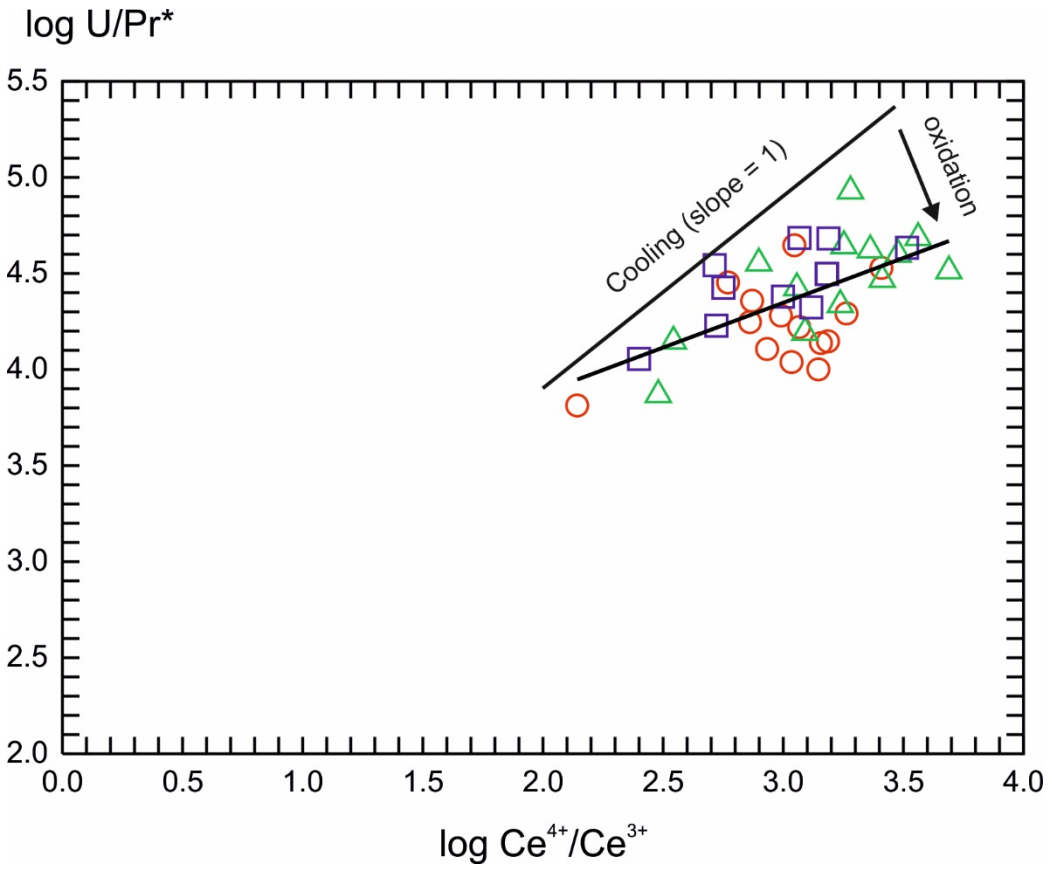

Figure S12 *Slope of the zircon composition array in the log Ce^{4+}/Ce^{3+} vs. log U/Pr* diagram (after Loucks et al. 2018). The regression slope suggests that the melt was undergoing oxidation*

The three studied eruptive units (Ee5/2-32, Ee5/1-50, and Ee5/1-56) contain zircon, which provided very similar crystallization condition. Temperature was estimated using the Ferry and Watson (2007) method for 30 zircon crystals. Temperature values lower than 680 °C were discarded (12 zircon grains) because of low Ti content, which is close to the detection limit and therefore has large uncertainty. The obtained temperature values are between 681 and 738 °C. In contrast, the Loucks et al. (2020) geothermometer yields a temperature value range of 725 and 813 °C because of the pressure dependence (at 250 MPa). The calculated fO_2 using the FW07 temperature and the Loucks et al. (2020) method is ranging between 0.35 and 1.55 ΔNNO.

The zircon saturation temperature was determined by two methods, using the Watson and Harrison (1983) and the more recent Crisp and Berry (2022) techniques. In both cases, we calculated the zircon saturation temperature based on the glass compositions (average of silicate melt inclusion and groundmass data) and the Zr content of the glassy groundmass. The WH83 method gave 780–785 °C for each eruptive unit, whereas the CB22 method yielded 768–796 °C.

4. Petrological and geochemical characteristics of the 133 ka Ciomadul Mic lava dome dacite

Here we introduce the main petrological and geochemical features of the 133 ka Ciomadul Mic lava dome dacite (Kiss et al. 2014) as a representative product of the effusive volcanism of Ciomadul. The main features along with those of the young pumices can be found in Table S2. In this section we report those minerals from the lava dome rocks which are important for their comparison with pumiceous deposits.

Plagioclase crystals (18 vol%, 10–4000 μm) in the Ciomadul Mic lava dome rocks show less variations in both texture and chemistry compared to the pumices. They form large (1.5–4 mm sized) crystals, clear euhedral glomerocrystic aggregates (not corroded) with amphibole, biotite, apatite and euhedral to subhedral, 100–250 μm sized titanite inclusions, large subhedral to anhedral crystals with sieved texture core, or euhedral microphenocrysts (not corroded) with overlapping compositional range (An= 26–56 mol%; Kiss et al. 2014). K-feldspar (<1 vol%, 10–4000 μm) is also present as embayed and rounded anhedral or subhedral macrocrysts with amphibole, biotite, plagioclase, and apatite inclusions and as microlites in the groundmass.

Felsic crystal clots are abundant with plagioclase as dominant phase in addition to low-Al amphibole, biotite, titanite, zircon and occasionally quartz. Anhedral and rounded

quartz (250–1250 μm sized) occurs as single crystals or with low-Al amphibole, plagioclase as well as titanite and zircon.

Euhedral to subhedral amphibole crystals (9 vol%, 75–1800 μm; with 6.4–15 wt% Al_2O_3 and 49–82 mol% Mg#; Kiss et al. 2014) in the Ciomadul Mic lava dome rocks typically have reaction rims with a maximum thickness of 15 μm, in contrast to the pumices, which contain amphibole without reaction rim. Kiss et al. (2014) found a bimodal composition of the amphiboles in the older lava dome rocks, a low-Al, low-Mg hornblende and a high-Al, high-Mg pargasite group (higher Al^{IV} at the same Mg# than in the pumices, Figure S3).

In the Ciomadul Mic dacite, mafic crystal clots are common with zoned olivine and clinopyroxene, which have high Mg-values (>85 mol%). They are occasionally overgrown by high-Al, high-Mg amphibole. These mafic crystals occur also as single crystals in the lava dome rocks. The clinopyroxene crystals (1%, 20–1250 μm) occur as subhedral-anhedral, patchy or complex normal zoned phases and also as euhedral to subhedral complex reverse zoned macrocrysts and crystal aggregates (400–1500 μm sized mafic crystal clots).

Titanite (<1 vol%) in dacites from the Ciomadul Mic dome-forming eruptions are complex zoned crystals. They form small, subhedral to euhedral 0.1–0.25 mm sized crystals enclosed by amphibole or plagioclase, but occur also as 1–4 mm sized subhedral to euhedral phenocrysts with biotite, apatite, and Fe-Ti oxide inclusions.

Zircon crystals (<0.1 vol%) in the Ciomadul Mic are ~300 μm sized, oscillatory zoned crystals, sometimes with an inherited core. They are mostly enclosed in amphibole, plagioclase, and felsic clots or form crystals in the groundmass.

Fe-Ti oxides (<0.1 vol%) are subhedral to anhedral, homogeneous or zoned, <100 μm sized crystals with resorbed cores in the Ciomadul Mic. They occur as inclusions in amphibole, biotite and plagioclase, and as groundmass crystals.

Method	Abbreviation	Phase(s)	Input	Output (used in this study)	Uncertainty	Macrocryst core/rim	Condition
Andersen and Lindsley (1985)	oxAL85	Fe-Ti oxides (mt-ilm eq. pairs)	EMPA	T fO_2	±20–40 °C ±0.50 log units	rim	pre-eruption
Holland and Blundy (1994)	hbHB94	amphibole-plagioclase eq. pairs	EMPA + P	T	±40 °C	core and rim	long-term storage (mush)/pre-eruption
Putirka (2016)	hbPu16	single amphiboles	EMPA	T, $melt_{SiO2}$	±30 °C ±3.6 wt%	core	mafic magma
Higgins et al. (2022)	hbHi22	single amphiboles	EMPA	P, T $melt_{SiO2, Al2O2}$	±160 MPa, ±40 °C ±3.3 wt% ±1.1 wt%	core	mafic magma
Hayden et al. (2008)	tiH08	titanite	LA-ICP-MS	T	±20 °C	core to rim	long-term storage (mush)
Anderson and Smith (1995)	hbAS95	amphibole-plagioclase eq. pairs	EMPA	P	±80 MPa	core	long-term storage (mush)
Mutch et al. (2016)	hbM16	amphibole-plagioclase eq. pairs	EMPA	P	±16 %	core	long-term storage (mush)
Médard and Le Pennec (2022)	hbMLP22	single amphiboles	EMPA	P	±72–86 MPa	core	long-term storage (mush)/pre-eruption
Krawczynski et al. (2012)	amKr12	single amphiboles	EMPA	P	±142 MPa	core	mafic magma
Ridolfi et al. (2010)	amR10	single amphiboles	EMPA T, P	fO_2	±0.4 log unit	core and rim	long-term storage (mush)/pre-eruption
Loucks et al. (2020)	zrL20	zircon	LA-ICP-MS T (Ferry and Watson 2007, P, a_{TiO2}, a_{SiO2}	fO_2	±0.6 log units	rim	long-term storage (mush)
Watson and Harrison (1983)	zrWH83	zircon	EMPA LA-ICP-MS Zr	$T_{saturation}$	2σ	rim	long-term storage (mush)
Crisp and Berry (2022)	zrCB22	zircon	EMPA LA-ICP-MS Zr P	$T_{saturation}$	±45 °C	rim	long-term storage (mush)
Waters and Lange (2015)	plWL15	plagioclase-melt pairs	EMPA + T, P	$melt_{H2O}$	±0.35 wt%	rim	pre-eruption
Erdmann et al. (2019)	tiE19	titanite	LA-ICP-MS	P	±60–100 MPa	rim	long-term storage (mush)
Arató and Audétat (2017a, b)	oxAA17V	magnetite-melt pairs	LA-ICP-MS	fO_2	±0.3 log units	magnetite rim, matrix glass	pre-eruption

Method	Abbreviation	Phase(s)	Input	Output (used in this study)	Uncertainty	Macrocryst core/rim	Condition
Arató and Audétat (2017c)	oxAA17FeTi	magnetite-melt pairs	EMPA	fO_2	±0.5 log units	magnetite rim, matrix glass	pre-eruption

Table S3 *Summary of the applied methods most relevant in the study (thermometers, barometers, oxybarometers, chemometers), indicating the phase(s) on which they are based, the necessary input data, and the inferred uncertainties of each method.*

References

Andersen DJ, Lindsley DH (1985) New (and final!) models for the Ti-magnetite/Ilmenite geothermometer and oxygen barometer. EOS Trans Am Geophys Union 66:416

Anderson JL, Smith DR (1995) The effects of temperature and fO2 on the Al-in-hornblende barometer. Amer Miner 80:549–559

Anderson JL, Barth AP, Wooden JL, Mazdab F (2008) Thermometers and thermobarometers in granitic systems. Rev Mineral Geochem 69:21–142. https://doi.org/10.2138/rmg.2008.69.4

Arató R, Audétat A (2017a) Vanadium magnetite–melt oxybarometry of natural, silicic magmas: a comparison of various oxybarometers and thermometers. Contrib Mineral Petrol 172:1–22. https://doi.org/10.1007/s00410-017-1369-6

Arató R, Audétat A (2017b) Experimental calibration of a new oxybarometer for silicic magmas based on vanadium partitioning between magnetite and silicate melt. Geochim Cosmochim Acta 209:284–295. https://doi.org/10.1016/j.gca.2017.04.020

Arató R, Audétat A (2017c) FeTiMM – A new oxybarometer for mafic to felsic magma. Geochem Perspect Lett 5:19–23. https://doi.org/10.7185/geochemlet.1740

Bacon CR, Hirschmann MM (1988) Mg/Mn partitioning as a test for equilibrium between Fe-Ti oxides. Amer Miner 73:57–61

Breiman L (2002) Manual on setting up, using, and understanding random forest V3.1. Statistics Department University of California. 1:58.

Crisp LJ, Berry AJ (2022) A new model for zircon saturation in silicate melts. Contrib Mineral Petrol 177:1–24. https://doi.org/10.1007/s00410-022-01925-6

Erdmann S, Martel C, Pichavant M, Kushnir A (2014) Amphibole as an archivist of magmatic crystallization conditions: problems, potential, and implications for inferring magma storage prior to the paroxysmal 2010 eruption of Mount Merapi, Indonesia. Contrib Mineral Petrol 167:1016. https://doi.org/10.1007/s00410-014-1016-4

Erdmann S, Wang R, Huang F, Scaillet B, Zhao K, Liu H, Chen Y, Faure M (2019) Titanite: a potential solidus barometer for granitic magma systems. CR Geosci 351:551–561. https://doi.org/10.1016/j.crte.2019.09.002

Ferry JM, Watson EB (2007) New thermodynamic models and revised calibrations for the Ti-in-zircon and Zr-in-rutile thermometers. Contrib Mineral Petrol 154:429–437. https://doi.org/10.1007/s00410-007-0201-0

Ghiorso MS, Evans BW (2008) Thermodynamics of rhombohedral oxide solid solutions and a revision of the Fe-Ti oxide geothermometer and oxygen-barometer. Amer J Sci 308:957–1039. https://doi.org/10.2475/09.2008.01

Ghiorso MS Gualda GAR (2013) A method for estimating the activity of titania in magmatic liquids from the compositions of coexisting rhombohedral and cubic iron–titanium oxides. Contrib Miner Petrol 165:73–81. https://doi.org/10.1007/s00410-012-0792-y

Gorini A, Ridolfi F, Piscaglia F, Taussi M, Renzulli A (2018). Application and reliability of calcic amphibole thermobarometry as inferred from calc-alkaline products of active geothermal areas in the Andes. J Volcanol Geotherm Res 358:58-76. https://doi.org/10.1016/j.jvolgeores.2018.03.018

Hawthorne FC, Oberti R, Harlow GE, Maresch WV, Martin RF, Schumacher JC, Welch MD (2012) Nomenclature of the amphibole supergroup. Am Min, 97:2031–2048. https://doi.org/10.2138/am.2012.4276

Hayden LA, Watson EB, Wark DA (2008) A thermobarometer for sphane (titanite). Contrib Mineral Petrol 155:529–540. https://doi.org/10.1007/s00410-007-0256-y

Hayden LA, Watson EB (2007) Rutile saturation in hydrous siliceous melts and its bearing on Ti-thermometry of quartz and zircon. Earth Planet Sci Lett 258:561–568.

Higgins O, Sheldrake T, Caricchi L (2022) Machine learning thermobarometry and chemometry using amphibole and clinopyroxene: a window into the roots of an arc volcano (Mount Liamuiga, Saint Kitts). Contrib Mineral Petrol 177:1–22. https://doi.org/10.1007/s00410-021-01874-6

Holland TJB, Blundy JD (1994) Non-ideal interactions in calcic amphiboles and their bearing on amphibole-plagioclase thermometry. Contrib Mineral Petrol 116:433–447. https://doi.org/10.1007/BF00310910

Jolles JS, Lange RA (2019) High-resolution Fe–Ti oxide thermometry applied to single-clast pumices from the Bishop Tuff: a re-examination of compositional variations in phenocryst phases with temperature. Contrib Mineral Petrol 174:1–43. https://doi.org/10.1007/s00410-019-1597-z

Kiss B, Harangi S, Ntaflos T, Mason PRD, Pál-Molnár E (2014) Amphibole perspective to unravel pre-eruptive processes and conditions in volcanic plumbing systems beneath intermediate arc volcanoes: a case study from Ciomadul volcano (SE Carpathians). Contrib Mineral Petrol 167:986. https://doi.org/10.1007/s00410-014-0986-6

Krawczynski MJ, Grove TL, Behrens H (2012) Amphibole stability in primitive arc magmas: effects of temperature, H2O content, and oxygen fugacity. Contrib Mineral Petrol 164:317–339. https://doi.org/10.1007/s00410-012-0740-x

Locock AJ (2014) An Excel spreadsheet to classify chemical analyses of amphiboles following the IMA 2012 recommendations. Comput Geosci, 62:1–11. https://doi.org/10.1016/j.cageo.2013.09.011

Loucks RR, Fiorentini ML, Rohrlach BD (2018) Divergent T–fO2 paths during crystallisation of H_2O-rich and H_2O-poor magmas as recorded by Ce and U in zircon, with implications for TitaniQ and TitaniZ geothermometry. Contrib Mineral Petrol 173:104. https://doi.org/10.1007/s00410-018-1529-3

Loucks RR, Fiorentini ML, Henríquez GJ (2020) New Magmatic Oxybarometer Using Trace Elements in Zircon. J Petrol 61, egaa034. https://doi.org/10.1093/petrology/egaa034

Lukács R, Caricchi L, Schmitt AK, Bachmann O, Karakas O, Guillong M, Molnár K, Seghedi I, Harangi S (2021) Zircon geochronology suggests a long-living and active magmatic system beneath the Ciomadul volcanic dome field (eastern-central Europe). Earth Planet Sci Lett 565:116965. https://doi.org/10.1016/j.epsl.2021.116965

Médard E, Le Pennec JL (2022) Petrologic imaging of the magma reservoirs that feed large silicic eruptions. Lithos 428:106812. https://doi.org/10.1016/j.lithos.2022.106812

Molnár K, Lukács R, Dunkl I, Schmitt AK, Kiss B, Seghedi I, Szepesi J, Harangi S (2019) Episodes of dormancy and eruption of the Late Pleistocene Ciomadul volcanic complex (Eastern Carpathians, Romania) constrained by zircon geochronology. J Volcanol Geotherm Res 373:133–147. https://doi.org/10.1016/j.jvolgeores.2019.01.025

Mutch EJF, Blundy JD, Tattitch BC, Cooper FJ, Brooker RA (2016) An experimental study of amphibole stability in low-pressure granitic magmas and a revised Al-in-hornblende geobarometer. Contrib Mineral Petrol 171:1–27. https://doi.org/10.1007/s00410-016-1298-9

Putirka K (2016) Amphibole thermometers and barometers for igneous systems and some implications for eruption mechanisms of felsic magmas at arc volcanoes. Amer Miner 101:841–858. https://doi.org/10.2138/am-2016-5506

Ridolfi F, Renzulli A, Puerini M (2010) Stability and chemical equilibrium of amphibole in calc-alkaline magmas: an overview, new thermobarometric formulations and application to subduction-related volcanoes. Contrib Mineral Petrol 160:45–66. https://doi.org/10.1007/s00410-009-0465-7

Ridolfi F, Renzulli A (2012) Calcic amphiboles in calc-alkaline and alkaline magmas: thermobarometric and chemometric empirical equations valid up to 1,130 °C and 2.2 GPa. Contrib Mineral Petrol 163:877–895. https://doi.org/10.1007/s00410-011-0704-6

Ridolfi F (2021) Amp-TB2: An Updated Model for Calcic Amphibole Thermobarometry. Minerals 11:324. https://doi.org/10.3390/min11030324

Stormer JC (1983) The effects of recalculation on estimates of temperature and oxygen fugacity from analyses of multicomponent-iron-titanium oxides. Amer Miner 68:586–594

Waters LE, Lange RA (2015) An updated calibration of the plagioclase-liquid hygrometer-thermometer applicable to basalts through rhyolites. Amer Miner 100:2172–2184. https://doi.org/10.2138/am-2015-5232

Watson EB, Harrison M (1983) Zircon Saturation Revisited: Temperature and Composition Effects in a Variety of Crustal Magma Types. Earth Planet Sci Lett 64:295–304

Yavuz F (2021) WinMIgob: A Windows program for magnetite-ilmenite geothermometer and oxygen barometer. J Geosci 66:51–70. http://doi.org/10.3190/jgeosci.319